Effect of the Andes Cordillera on Precipitation from a Midlatitude Cold Front

BRADFORD S. BARRETT

Department of Oceanography, U.S. Naval Academy, Annapolis, Maryland

RENÉ D. GARREAUD AND MARK FALVEY

Department of Geophysics, Universidad de Chile, Santiago, Chile

(Manuscript received 24 November 2008, in final form 23 March 2009)

ABSTRACT

The effects of the Andes Cordillera, the major mountain range in South America, on precipitation patterns of baroclinic systems approaching from the southeast Pacific remain largely unstudied. This study focuses on a case in late May 2008 when an upper-level trough and surface cold front produced widespread precipitation in central Chile. The primary goal was to analyze the physical mechanisms responsible for the structure and evolution of the precipitation.

Weather Research and Forecasting (WRF) model simulations indicate that as an upper-level trough approached central Chile, midtropospheric flow below 700 hPa was blocked by the high topography and deflected poleward in the form of a barrier jet. This northerly jet had wind maxima in excess of 15 m s^{-1}, was centered around 925 hPa, and extended westward 200 km from the mountains. It intersected the cold front, which approached from the south near the coast, thereby increasing convergence along the frontal surface, slowing its equatorward progress, and enhancing rainfall over central Chile. Another separate region of heavy precipitation formed over the upwind slopes of the cordillera. A trajectory analysis confirmed that the barrier jet moved low-level parcels from their origin in the moist southeast Pacific boundary layer to the coast. When model topography was reduced to twenty percent of its original height, the cold front advanced more rapidly to the northeast, generated less precipitation in central Chile between 33° and 36°S, and produced minimal orographic precipitation on the upwind Andean slopes. Based on these findings, the high topography appears responsible for not only orographic precipitation but also for substantially increasing precipitation totals over the central coast and valley.

1. Introduction

The Andes cordillera is the major mountain range in the Southern Hemisphere. It extends for more than 5000 km along the west coast of South America, from north of the equator to the southern tip of the continent, with mean heights ranging from 1000–1500 m MSL in the midlatitudes to up to 5000 m MSL at subtropical and equatorial latitudes, and its cross-mountain scale is about 200 km. The Andes impact tropospheric circulation on a broad range of scales, from the generation of mesoscale eddies (e.g., Garreaud et al. 2002) to the disruption of weather systems (e.g., Seluchi et al. 2006; Garreaud and Fuenzalida 2007) to the organization of the South American monsoon system (e.g., Vera et al. 2006). The systems impinging the southern portion of the continent are embedded in the South Pacific storm track, the axis of which is located between 40° and 50°S throughout the year (Trenberth 1991; Hoskins and Hodges 2005). Much attention has been devoted to the channeling effects of surface anticyclones along the east (downstream) side of the Andes that lead to rapid incursions of cold air that may reach as far north as the Amazon basin (Garreaud 2000; Lupo et al. 2001; Seluchi et al. 2006). The disruption of weather systems, particularly cold fronts, along the west (*upstream*) side of the extratropical Andes has been less studied, in part because of the lack of data over the adjacent Pacific Ocean.

Orographic influences on frontal systems have been studied previously in other locations around the world. One of the most prominent effects of mountains on the lower atmosphere is ''upstream blocking'' (Yu and Smull 2000). For the case of a steep, nearly two-dimensional

Corresponding author address: Bradford S. Barrett, Department of Oceanography, U.S. Naval Academy, 572C Holloway Road, Annapolis, MD 21403.
E-mail: bbarrett@usna.edu

DOI: 10.1175/2009MWR2881.1

barrier, such as that presented by the central Andes, a major result of upstream blocking is the development of strong low-level flow parallel to the terrain axis (Parish 1982) resulting from downgradient ageostrophic acceleration in the along-barrier direction (Overland 1984; Lackmann and Overland 1989). These ''barrier jet'' wind maxima are often supergeostrophic (Marwitz 1987; Overland and Bond 1993) and enhanced by cold air damming effects (e.g., Bell and Bosart 1988; Doyle and Warner 1993). Low-level blocking is common when flow normal to the terrain axis is characterized by a large Nh/U regime (a regime with a Froude number smaller than the critical threshold of 1.0), where N is the buoyancy frequency, h is the height of the mountain, and U is the speed of the free airstream (Pierrehumbert and Wyman 1985; Overland and Bond 1995; Doyle 1997).

Although the mesoscale details of topography–frontal interactions are complex, a commonly observed modification is the deformation and deceleration of surface fronts and precipitation upstream of the high terrain (Neiman et al. 2004). Bjerknes and Solberg (1921) were among the first to observe this phenomenon, noting that a warm front deformed as it approached coastal Norway, with the lower tropospheric portion precluded from crossing the complex topography. More recent observations in the Olympic Mountains of western Washington State documented the development of strong poleward surface winds as cold fronts approached the coastal range because of mesoscale pressure ridging upstream of the topography (Mass and Ferber 1990). A similar low-level, prefrontal wind maximum was observed adjacent to the steep terrain along the central California coast (Doyle 1997) and just west of the Sierra Nevada (Marwitz 1987). Other observations of fronts decelerated by upstream flow blocked by topography have been made in the European Alps (e.g., Kurz 1990), the Appalachian Mountains (O'Handley and Bosart 1996), the coastal mountains of western Canada (Doyle and Bond 2001), the Wasatch mountains of northern Utah (Cox et al. 2005), and the Pacific Northwest (Braun et al. 1999; Yu and Bond 2002). Precipitation distribution in the Alps and Apennines has also been related to both the degree of flow blocking by topography (e.g., Medina and Houze 2003) and the amount of entrainment of moist low-level air into unblocked flow aloft (e.g., Bousquet and Smull 2006). Prefrontal low-level blocking has been observed to aid rapid weakening of a cold front as it approached the Pacific Cascades (Bond et al. 2005), and topographic barrier jets have been observed by synthetic aperture radar in the Gulf of Alaska (Winstead et al. 2006). In addition to these observational studies, there are multiple theoretical experiments that describe the inverse relationship between the Froude number and the degree of frontal retardation (e.g., Egger and Hoinka 1992). Furthermore, several studies have used numerical simulations with and without topography to evaluate the role of terrain (e.g., Buzzi et al. 1998; Rotunno and Ferretti 2001).

In the broadest sense, the Andes south of 30°S exhibit a typical rainfall pattern for a midlatitude mountain range: a relatively wet upwind side and relatively dry region downwind (e.g., Smith 1979a; Roe 2005). Around 40°S, for instance, annual mean precipitation varies from 2000–3000 mm along the Pacific (Chilean) coast and western slope of the Andes to less than 200 mm just to the east of the continental divide over Argentinean Patagonia (Fuenzalida 1982)—a distance of less than 300 km in the zonal direction. Such a marked west–east gradient is often mentioned as a classical example of upslope rain enhancement and downslope rain shadow effects (e.g., Smith 1979b; Smith and Evans 2007). Furthermore, the local midtropospheric zonal flow exhibits a significant, positive (negative) correlation with precipitation west (east) of the Andes on both the synoptic scale (Falvey and Garreaud 2007) and climate time scales (Garreaud 2007).

A marked north–south precipitation gradient is also observed along the west side of the Andes cordillera. Records from coastal and inland stations in central Chile show a steep increase from about 100 mm $year^{-1}$ at 30°S up to 2000 mm yr^{-1} at 40°S (Montecinos and Aceituno 2003), leading to a transition from arid conditions to rain forests. This meridional precipitation gradient is collocated with a gradient in terrain elevation: the Andes mean height *decreases* from about 4500 m MSL at 30°S down to 1500 m MSL at 40°S. Some authors in the geological community have speculated that the inverse relationship between precipitation and the Andes' elevation is rooted in a long-term relationship between climate, erosion, and tectonics [see Farías et al. (2008) for a review]. The narrow strip of land between the Andes and the Pacific coast also concentrates about 10 million inhabitants, about 70% of the Chilean population, so understanding the orographic control of precipitation along central Chile is an important practical issue.

To advance in our understanding of the upstream influence of the Andes on midlatitude weather systems and hence on precipitation distribution, in this study we examine the structural evolution of a cold front that passed over central Chile in May (late fall) 2008. As shown later, the event had typical features and produced 30–50 mm of rainfall in central Chile. Our analysis is based on in situ and satellite data as well as on the results from two mesoscale numerical simulations (one control simulation and one with reduced topography) performed with the Weather and Research Forecast (WRF) model

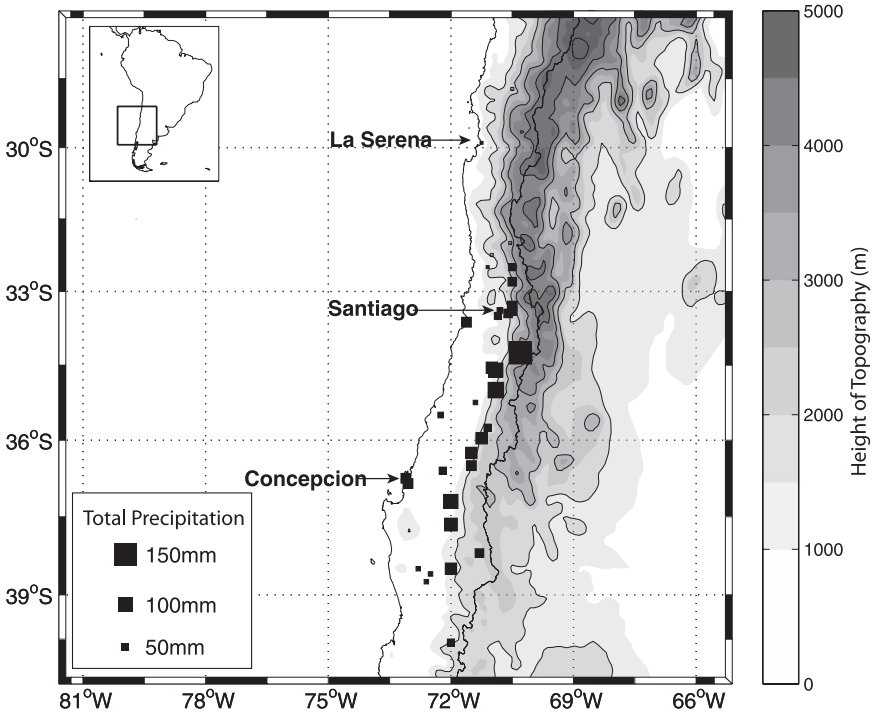

FIG. 1. Terrain height (m MSL) for the control simulation. Black squares indicate the locations of the 41 observing stations, and square size indicates the amount of precipitation that fell during the cold front passage during 25–29 May 2008. Time series of temperature, dewpoint, and air pressure are presented in Fig. 4 for Concepcion, Santiago, and La Serena.

(Skamarock et al. 2005). The remainder of the article is organized as follows: Synoptic and mesoscale observations of the event are presented in section 2. Section 3 describes the model control and sensitivity experiments, and model output is analyzed in section 4. Our conclusions are presented in section 5.

2. Episode overview

In this section, we present a surface and upper-air overview of the cold front passage in central Chile from 25 to 28 May 2008. We selected this case because it represents a common autumn–winter synoptic pattern: a positively tilted midlevel trough approached subtropical South America, promoted frontogenesis along and offshore of the Chilean coast, and led to widespread precipitation in central Chile. We base our analysis on Geostationary Operational Environmental Satellite-12 (*GOES-12*) visible images, upper-air data from the National Centers for Environmental Prediction (NCEP)–National Center for Atmospheric Research (NCAR) Reanalysis (Kalnay et al. 1996), and surface observations from a total of 41 stations in central-south Chile operated by the National Weather Service (28 stations), National Water Bureau (12 stations), and the Universidad de Chile (1 station). Figure 1 shows the locations of the observing stations, the total precipitation recorded at each station during the period, and the topography of the region.

At 1800 UTC 25 May 2008 there were two primary upper-air features over South America. First, a trough axis at 500 hPa extended from a vorticity maximum centered near 40°S, 85°W southeastward to the Antarctic Peninsula (Fig. 2a). Second, zonal (cross-barrier) 500-hPa flow with speeds between 15 and 30 m s^{-1} was impinging on the central and south-central Chilean Andes from 30°S to 45°S. At the surface, a cold front was identifiable in visible satellite imagery as a band of low and middle clouds extending from near 38°S, 72°W northwestward to 35°S, 85°W (Fig. 2a). This east–west baroclinic zone between the cold anticyclone and the warm subtropical air extended west from the Chilean coast 1200 km into the southeast Pacific. By 1800 UTC 27 May 2008, the 500-hPa vorticity maximum over the southeast Pacific had moved eastward to a position along the cordillera near 40°S and phased with a large closed low east of Argentina in the South Atlantic (Fig. 2b). A positively tilted trough axis extended northwestward from this vorticity maximum into the southeast Pacific. An extensive area of shallow open cloud cells

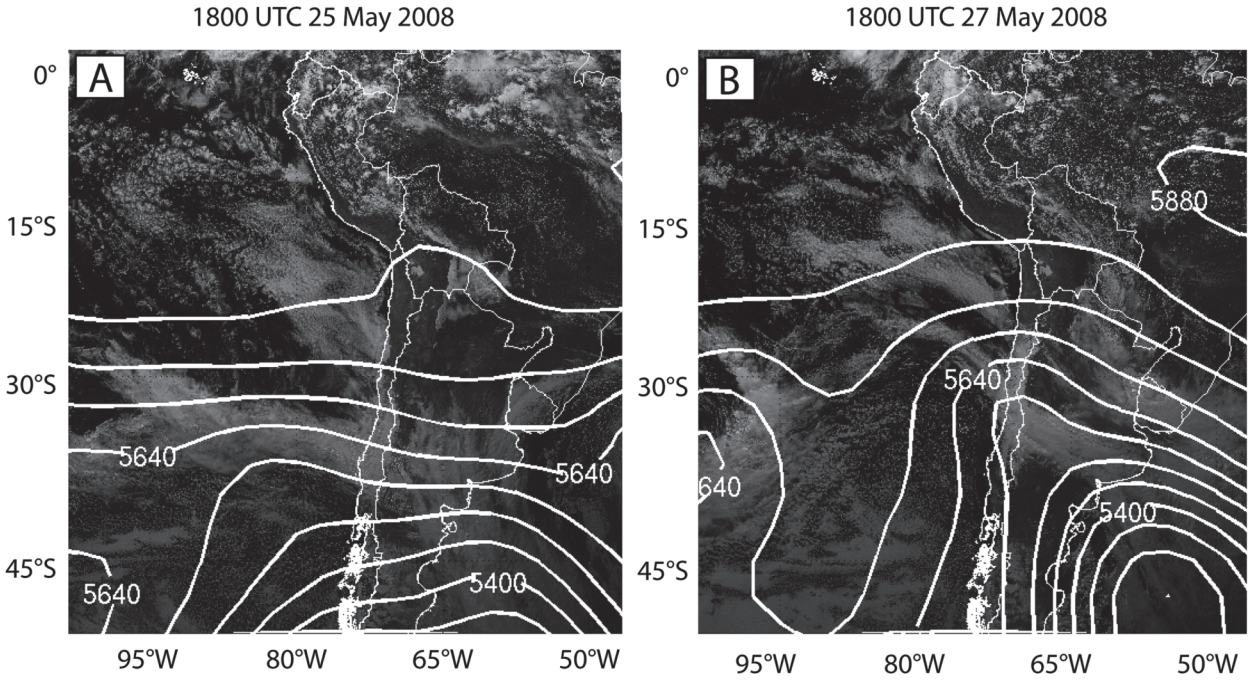

FIG. 2. *GOES-12* visible satellite image and NCEP–NCAR 500-hPa reanalysis geopotential height overlay at 1800 UTC (a) 25 May and (b) 27 May. Heights are contoured every 60 m.

dominated off southern Chile, indicative of very cold low-level air moving behind the front (Fig. 2b). A well-defined band of cumulus clouds (Fig. 2b) identified the position of the cold front and extended from near 30°S, 80°W in the southeast Pacific southeastward to the Andes cordillera, where it then continued eastward into western Argentina. Surface reanalysis showed a large and intense (1035 hPa) cold-core (5°–7°C) postfrontal anticyclone over the southeast Pacific (not shown). This surface anticyclone was connected to a marked high-amplitude midatmospheric ridge extending to 50°S along 95°W.

The cold front was also observed by the Quick Scatterometer (QuikSCAT; Ebuchi et al. 2002; Leslie et al. 2008) and the Tropical Rainfall Measuring Mission (TRMM; Simpson et al. 1996) Microwave Imager (TMI; Kummerow et al. 1998) satellite instruments (Figs. 3a–d). The QuikSCAT data revealed a well-defined wind shift associated with the cold front, oriented from southeast to northwest offshore central Chile on 26 May (Fig. 3a), and confirmed that this wind shift progressed equatorward, passing north of 27°S after 28 May (Fig. 3d). The open-ocean section of this wind shift maintained a southeast to northwest orientation as it advanced northeastward. However, the alongshore section, which was initially oriented south-southeast to north-northwest, deformed over time and became nearly parallel to the Chilean coast. As a result, this section of the front did not advance as rapidly equatorward as the open-ocean section. TMI rainfall data confirmed that a region of precipitation trailed the wind shift by about 100 km over the southeast Pacific on 26 May (Fig. 3a). This precipitation region was observed to advance equatorward with the wind shift and diminish in intensity (Fig. 3b), eventually dissipating by 27 May (Fig. 3c). The decline in precipitation intensity is consistent with the weakening of quasigeostrophic forcing that occurred after the upper-level trough axis passed to the east of the surface front. The cold front also likely weakened as the postfrontal air moved over progressively warmer sea surface temperatures as it moved equatorward (e.g., DiMego et al. 1976).

We also examined the progress of the cold front in time series of temperature, dewpoint temperature, and air pressure at three surface stations. Observations from Concepción, Santiago, and La Serena (see Fig. 1) showed that although the cold front progressed northward along the coastal and central valley of Chile, its strength—measured by changes in temperature, dewpoint temperature, and pressure—and total precipitation gradually diminished, especially north of Santiago. The front arrived first at Concepción and was followed by a 10°C drop in dewpoint temperatures, an 8-mb rise in surface pressure, and a 3°C drop in surface temperature over approximately the next 12 h (Figs. 4a–c). A total of 63 mm fell at Concepción, beginning by 1800 UTC 25 May and ending around 0000 UTC 27 May, about the

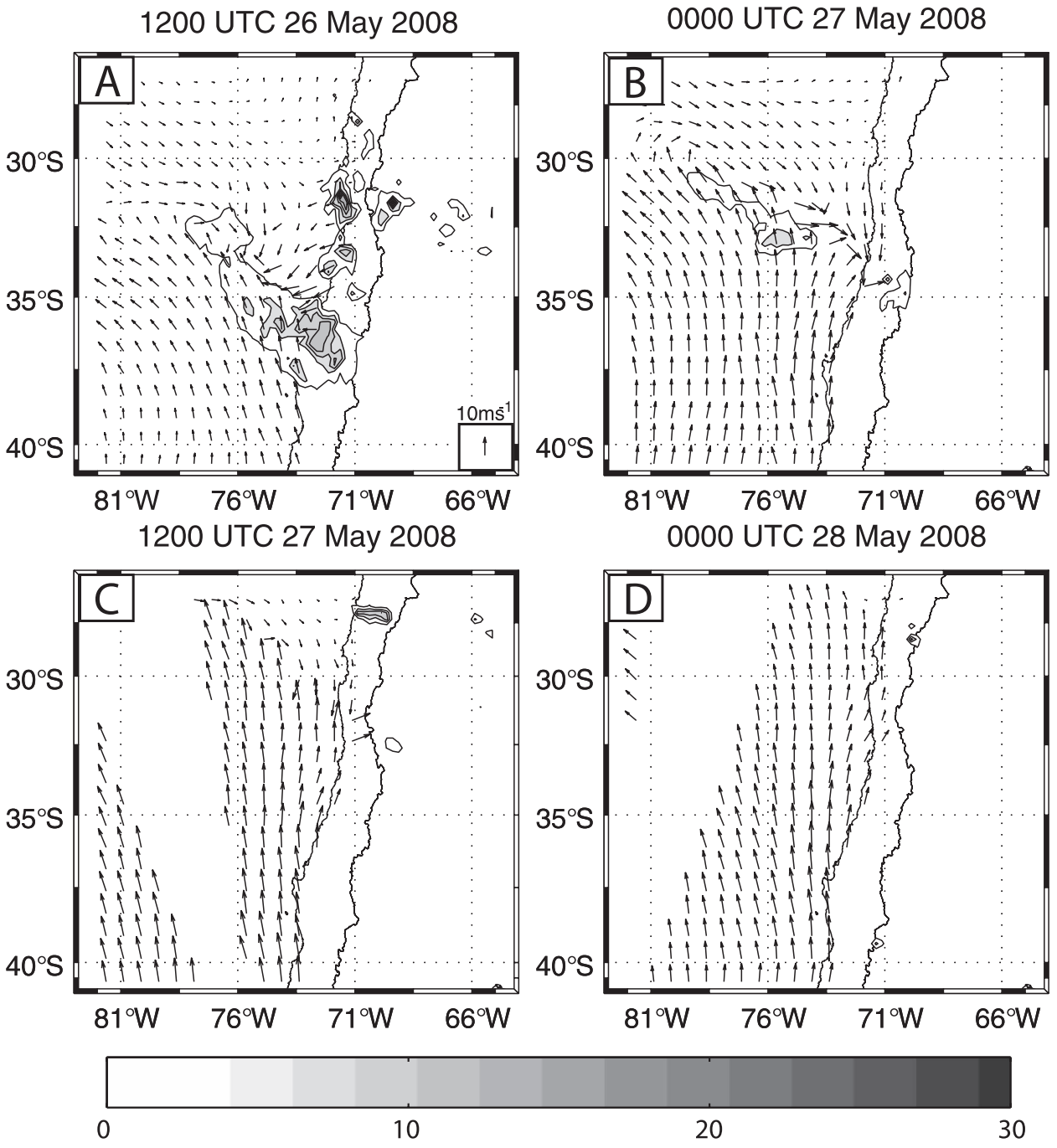

FIG. 3. QuikSCAT surface wind and TRMM 3-h rainfall rate (mm; contoured every 2 mm) observations every 12 h from 1200 UTC 26 May to 0000 UTC 28 May. Wind speed is scaled to 10 m s^{-1}.

time of cold front passage. Farther north at Santiago, the cold front arrived around 1800 UTC 27 May, evidenced by a temperature drop from 11° to 6°C, a 4-hPa rise in pressure, and a 6°C decrease in dewpoint temperature over the next 12 h. Rainfall began shortly after 1700 UTC 26 May and continued until about 0100 UTC 28 May, accumulating 43 mm in 36 h. At La Serena, the northernmost of the three stations in this analysis, a temperature decrease of 4°C, dewpoint decrease of 2.5°C, and pressure rise of 4 mb were recorded in the 12 h following frontal passage, and only 7 mm of precipitation was measured. The rainfall totals, temperature and dewpoint change, and pressure rise were all less at Santiago than at Concepción, indicating that the cold front was

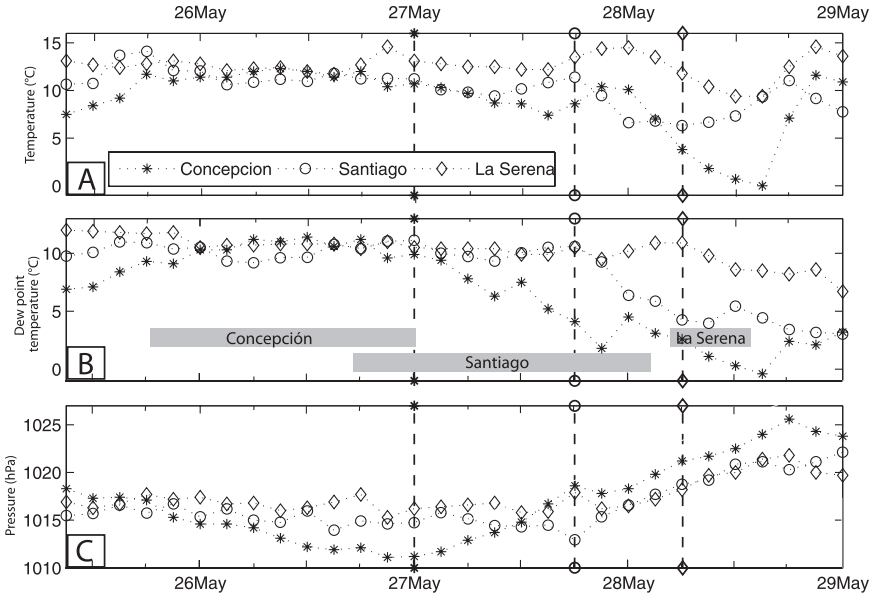

FIG. 4. Time series of (a) temperature (°C), (b) dewpoint temperature (°C), and (c) station air pressure (mb) at Concepción (asterisks), Santiago (circles), and La Serena (diamonds) from 1200 UTC 25 May to 0000 UTC 29 May. Frontal passage, indicated by the dotted lines, occurred at Concepción first, then Santiago, and finally at La Serena. Gray sections in (b) indicate duration of observed rainfall. Station locations are given in Fig. 1.

weakening as it progressed northward. Other surface stations also reflect this precipitation pattern, with southern sites near Concepción receiving 60–80 mm of event-total rainfall, locations near Santiago receiving between 40–60 mm, and stations near La Serena receiving less than 10 mm (Fig. 1). A maximum of 150 mm was measured at an elevation of 1500 m in the cordillera southeast of Santiago. Furthermore, most of the precipitation fell before the frontal passage in the south and after the frontal passage in the north.

3. Model description

To better understand the temporal and spatial evolution of this precipitation event, we ran a 72-h simulation using version 2.2 of the Advanced Research Weather Research and Forecasting Model (ARW-WRF, or simply WRF; Skamarock et al. 2005), initialized at 1200 UTC 25 May 2008, about 24 h before the onset of precipitation in central Chile. The single-domain forecast was centered at 35°S, 75°W with 351 grid points in the *x* direction and 350 grid points in the *y* direction at a horizontal resolution of 10 km and a time step of 50 s (see Fig. 1 for an outline of the model domain). The model top was prescribed as 50 hPa and vertical sigma-level resolution decreased from 15 hPa near the surface to 60 hPa at the model top, yielding 24 unevenly spaced half-sigma levels. The initial and lateral boundary conditions were obtained every 6 h from the NCEP Global Forecasting System (GFS; Caplan and Pan 2000) with 1° horizontal resolution. Additional physical parameterization choices are summarized in Table 1.

To isolate the impact of the high cordillera on the evolution of the front as well as the magnitude and distribution of frontal precipitation, two simulations of the event were performed: a control (CTL) simulation, with full topography and all the choices discussed above and in Table 1, and an experiment (LOW) with topography over the entire domain reduced to 20% of the control. The LOW simulation allowed us to uniformly reduce the topography but still maintain its original structure with heights decreasing from north to south. In the LOW simulation, initial conditions were interpolated in space to create the subterranean data. Other than the topography, all other model characteristics in LOW, including the physics options, were kept equal to CTL.

4. Model results

a. Evolution of precipitation features

A qualitative analysis of the temporal evolution of the 3-h precipitation, 975-hPa wind, and 500-hPa geopotential height from the CTL simulation (Fig. 5) revealed that three primary precipitation features were associated with this event: a Pacific precipitation zone (PPZ), located over the southeast Pacific west of the

TABLE 1. Summary of physical parameterization selections used in the WRF control and low topography simulations.

Physical parameterization		Reference(s)
Radiation	Shortwave: Goddard Longwave: Rapid Radiative Transfer Model (RRTM) Time step: 30 min	Chou and Suarez (1994); Mlawer et al. (1997)
Microphysics	Purdue–Lin	Lin et al. (1983)
Subgrid-scale precipitation	Kain–Fritsch	Kain and Fritsch (1993)
Surface layer processes	Monin–Obukhov–Janjić, Noah land surface model	Janjić (1996, 2002); Chen and Dudhia (2001)
Turbulence kinetic energy	Mellor–Yamada–Janjić	Mellor and Yamada (1982); Janjić (2001)

Chilean coast; a coastal precipitation zone (CPZ), extending from the eastern edge of the PPZ along the Chilean coast eastward to the Andes Cordillera; and an windward precipitation zone (WPZ), located over the high Andean terrain. As we will show, the structure and evolution of each precipitation feature was directly related to the structure and evolution of the lower and midtropospheric wind field, including a topographically forced barrier jet.

At the start of the CTL simulation, the PPZ was located over the southeast Pacific west of Chile and was oriented from southeast to northwest with precipitation rates of 2–3 mm h^{-1} (Fig. 5a). The CPZ, in contrast, was located along the central Chilean coast and had a more meridional orientation and precipitation rates between 3 and 5 mm h^{-1}. The PPZ joined the CPZ 50 km west of the coast, and the two features remained connected throughout the remainder of the CTL simulation. The PPZ maintained a southeast to northwest orientation and advanced steadily equatorward (Figs. 5b–d) and (as discussed in section 2) after passing north of 27°S on 28 May, its precipitation intensity diminished. A schematic of the three precipitation features is noted in Fig. 5b.

In contrast to the PPZ, the CPZ advanced equatorward more slowly, stalling over central Chile at about 36°S during 26 May with precipitation rates from 5 to 10 mm h^{-1} (Fig. 5b). By 1200 UTC 28 May, the CPZ had become oriented nearly parallel to the coast (Fig. 5d). This change in orientation is physically consistent with similar cold front–terrain interactions observed off the California coast (e.g., Doyle 1997; James and Houze 2005) and suggests that the features observed in California, including a topographically forced barrier jet, may have also been present in central Chile. The WPZ formed in advance of the front and was well developed over the Chilean cordillera (Fig. 5b) by 1800 UTC 26 May as zonal wind speeds increased and static stability decreased ahead of the approaching upper-level trough. These two factors combined to increase Froude numbers for parcels above 700 hPa above a critical threshold of 1.0 (e.g., Egger and Hoinka 1992) and to allow them to cross the orographic barrier. Initial orographic precipitation intensities ranged from 1 to 2 mm h^{-1}. By 1800 UTC 27 May, the WPZ covered a large north–south portion (over 600 km) of the western Cordillera above 3000 m with precipitation rates over 10 mm h^{-1} (Fig. 5c) Similar to the coastal CPZ, the WPZ did not advance northward as rapidly as the PPZ, remaining roughly between 30°S and 36°S throughout the remainder of the event as strong cross-barrier flow and low atmospheric stability prevailed ahead of the upper-level trough axis.

b. Time–space plots

We now examine the structure and evolution of the three precipitation features through a series of time–longitude and time–latitude plots. An east–west time–longitude plot along 33°S (selected because that parallel intersects with each of the three precipitation features during the CTL simulation) clearly shows both the PPZ, which moved eastward in time, and the WPZ, which formed just after 0000 UTC 26 May and remained stationary over the mountains near 70°W throughout the remainder of the simulation (Fig. 6a). The slope of the isohyets shows that the core of the PPZ advanced eastward about 6° day^{-1}, or 600 km day^{-1}. Precipitation intensities along the PPZ remained steady for the first half of the simulation as the open-ocean portion of the front advanced equatorward. An east–west time–latitude cross section of the 700-hPa u-wind component along 33°S (Fig. 6c) shows similarity between midlevel zonal velocities and the intensity and evolution of the PPZ and WPZ (Fig. 6a). For example, the eastward progression of wind speeds above 15 m s^{-1} matched almost exactly the location and eastward progression of the PPZ. Furthermore, 700 hPa u-wind maxima greater than 20 m s^{-1} were aligned along the cordillera near 70°W, similar to the alignment of the WPZ in Fig. 6a (the region between 69° and 70.5°W at 700 hPa is below ground, hence the small gap in Fig. 6c). This relationship between stronger midtropospheric westerly flow and surface precipitation agrees with Falvey and Garreaud (2007), who found that

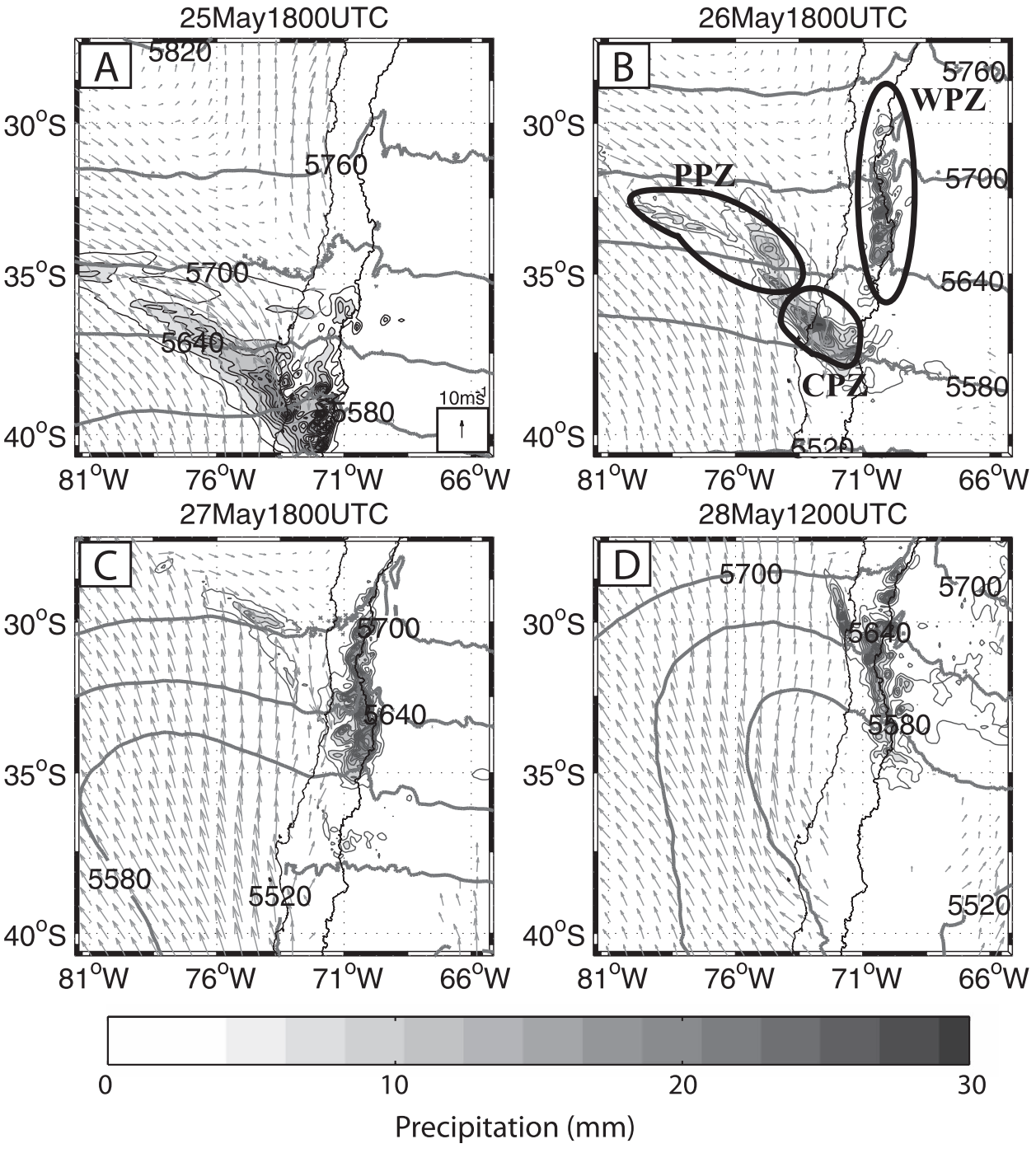

FIG. 5. CTL simulation output of 3-h precipitation totals, 975-hPa wind, and 500-hPa geopotential height. Wind speed is scaled to 10 m s^{-1} and geopotential height is contoured every 60 m. The three precipitation features are identified in (b): the Pacific precipitation zone (PPZ) located over the southeast Pacific, the coastal precipitation zone (CPZ) located over the Chilean coast and central valley, and the windward precipitation zone (WPZ) located over the high cordillera along the Chile–Argentina border.

central Chile precipitation was most strongly correlated with the 700 hPa *u*-wind component.

A north–south time–latitude plot of precipitation along the Chilean coast more clearly shows the full evolution of the CPZ. This precipitation feature advanced northward an average of 350 km day^{-1} (half as fast as the PPZ), reaching 30°S by the end of the simulation (Fig. 6b). Note that the CPZ stalled around 36°S for

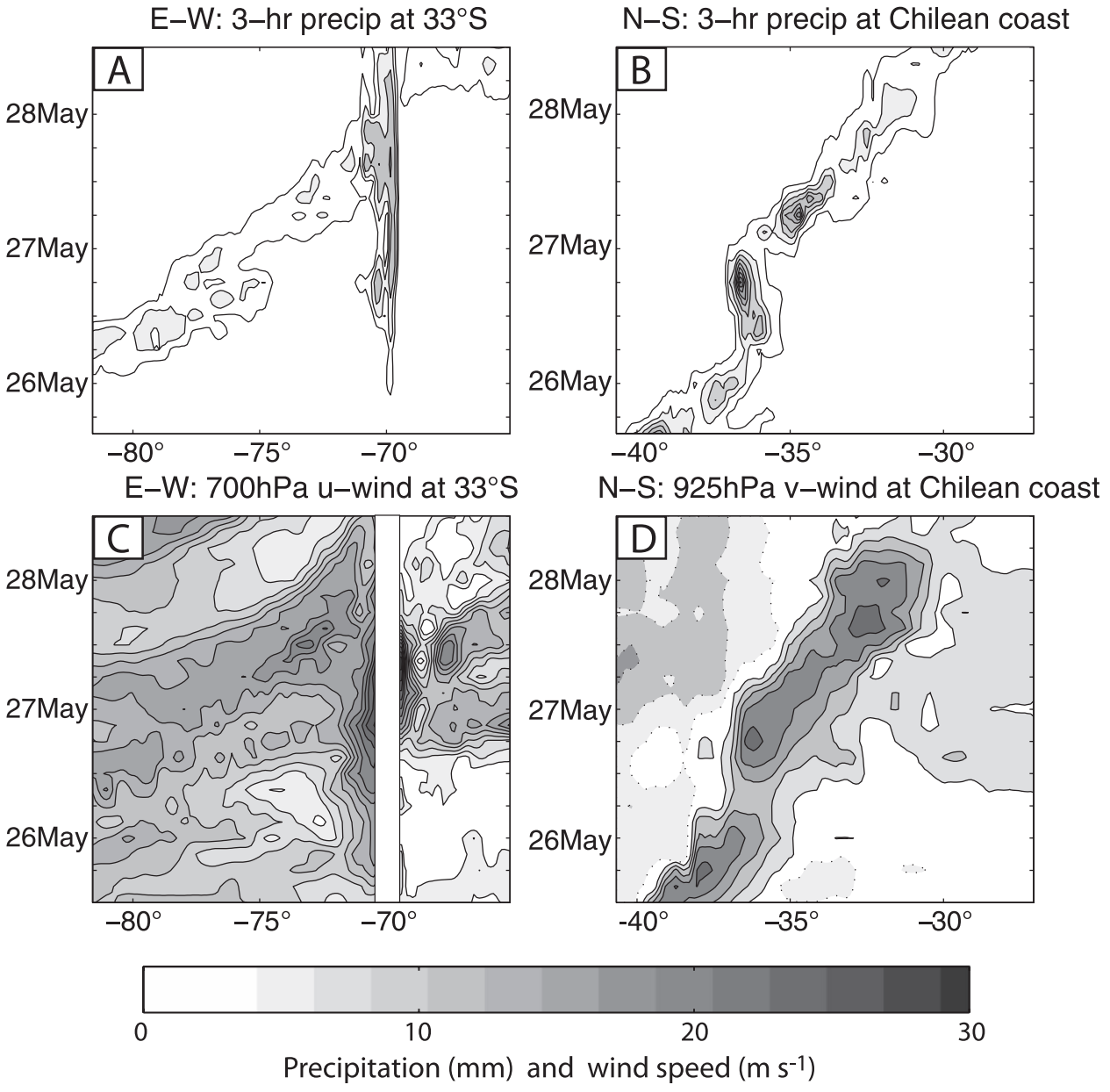

FIG. 6. CTL simulation cross sections of (a) east–west 3-h precipitation (mm) along 33°S, (b) north–south 3-h precipitation (mm) along the coast, (c) east–west 700 hPa u wind along 33°S (m s^{-1}), and (d) north–south coastal 925 hPa v wind (m s^{-1}). Wind speed in (c) and (d) is shaded every 5 m s^{-1}. In (c), part of the topography extends above 700 hPa and is indicated by the white bar. In (d), stippled contours indicate southerly flow. Longitude for (a) and (c) follows the coastline and ranges from 70° to 72°W.

18 h on May 26. During this period, precipitation intensities reached their maximum and ranged from 6 to 10 mm h^{-1}. Surface stations in the vicinity of Concepción (located near 36°S) confirmed this peak in precipitation, recording nearly all their event total precipitation (between 40 and 80 mm) during this 18-h period. After resuming its northward progress along the coast, precipitation intensities peaked again near 33°–34°S on 27 May, and this peak was also confirmed by surface observations in the region. After passing north of 33°S, precipitation along the CPZ diminished in intensity.

A north–south time–latitude plot of the 925-hPa v-wind component along the Chilean coast (Fig. 6d) shows the evolution of low-level wind. The location, structure, and evolution of this wind maximum were very similar to those of the precipitation (Fig. 6b). For example, a maximum in northerly flow (speeds greater

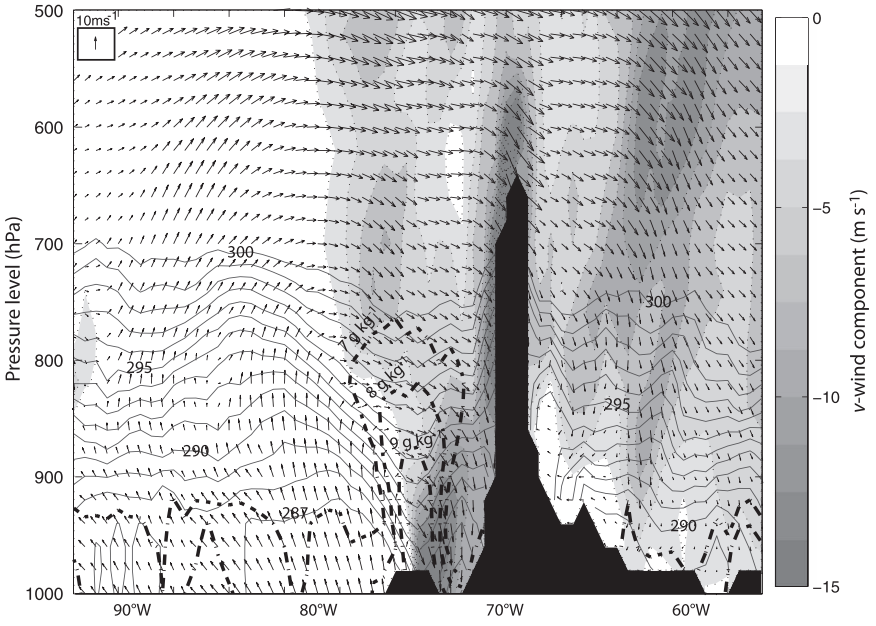

FIG. 7. Longitude–height cross section of horizontal wind (vectors, with v wind shaded), potential temperature (thin black lines), and specific humidity (thick dashed lines) at 34°S on 27 May 2008. The near-surface northerly barrier jet is well defined between the mountains and 75°W and between the surface and 850 hPa. The western half of the barrier jet is collocated with a maximum in specific humidity, indicating moisture transport from the subtropical Pacific to the north.

than 15 m s^{-1}) advanced steadily northward until 0600 UTC 26 May, stalled for 18 h around 36°S, and then continued advancing northward (Fig. 6d), very similar to the evolution of the CPZ (Fig. 6b). Wind maxima in the northerly flow corresponded, in both timing and location, to the greatest precipitation intensity of the CPZ. Additionally, where northerly flow was weaker, including north of 33°S, precipitation intensity along the CPZ was also weaker. A longitude–height cross section along 34°S reveals that the northerly flow was characterized by wind speeds above 15 m s^{-1}, that it was located immediately to the west of the cordillera, and that it was centered above the frontal surface between 850 and 950 hPa (Fig. 7). A maximum in specific humidity (>10 g kg^{-1}) was collocated with this wind maximum, indicating poleward transport of moisture from the subtropics.

A well-defined region of low-level convergence in the 925-hPa wind field moved equatorward with the coastal front and CPZ from 25 to 28 May 2008 (Fig. 8). The strongest low-level convergence was centered at the intersection of the PPZ and CPZ and extended east to the cordillera. The convergence was greatest near Concepción on 25 May 2008 (Fig. 8a) and Santiago on 27 May 2008 (Fig. 8c) and weakened as the CPZ approached La Serena (Fig. 8d). This low-level convergence is additional evidence of a northerly barrier jet that formed in response to lower-atmospheric flow blocking by the Andes. The westerly low and midtropospheric flow (Fig. 6a) helped to force this barrier jet (Figs. 6c and 7) and resulted in enhanced precipitation in the CPZ (Fig. 6d) and low-level convergence (Fig. 8) on its southern end. This setup is similar to observations from an event off Vancouver Island, although the low-level flow in that region extended only 20 km from the coast and was confined to the lowest 1.5 km of the troposphere (Yu and Bond 2002).

c. Trajectories

In this subsection we use a parcel trajectory analysis to further diagnose the forcing for precipitation, as well as the air mass source region and vertical motion. Using a simple, three-dimensional advective technique, we produced backward and forward trajectories at all model sigma levels for two locations, one along the coast at the northern edge of the CPZ (Fig. 9) and the other along over the cordillera in the WPZ (Fig. 10). The trajectories were calculated backward for the 24 h leading up 1800 UTC 26 May and forward for the 24 h following. Parcels that approached the point just north of the cold front (Fig. 9) clustered into two main groups. The parcels below 1500 m approached first from the northwest and then from the north, originally following the synoptic northwesterly flow over the southeast Pacific before turning

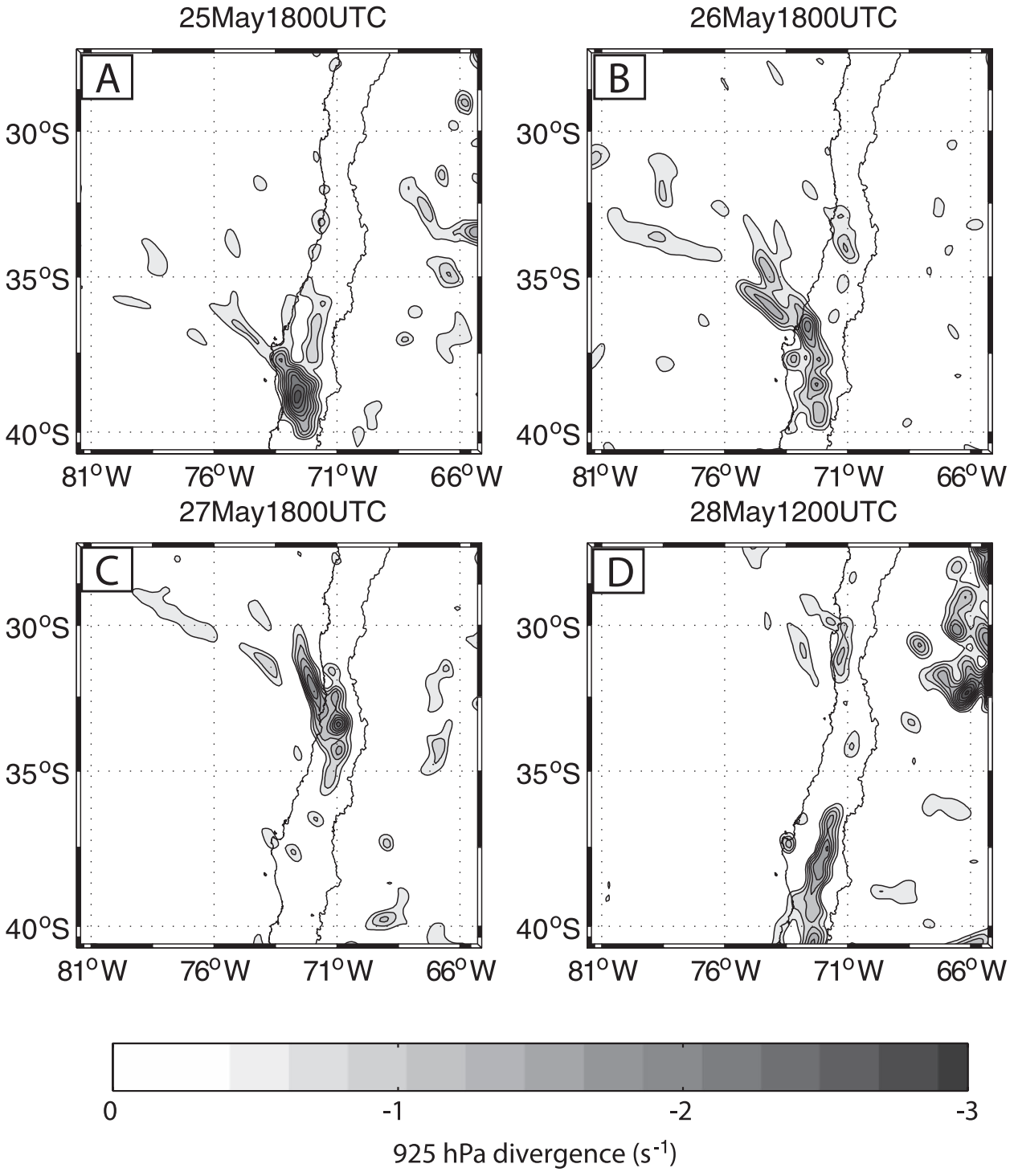

FIG. 8. Low-level (925 hPa) wind divergence (s^{-1}). Negative values represent regions of convergence. Strongest convergence followed the CPZ northward along the coast and weakened as it moved equatorward.

south as they encountered the northerly barrier jet close to the coast (Fig. 9a, open circles). These parcels either maintained their height or rose slightly as they traversed the southeast Pacific northwest of the front, but once they reached the CPZ (rainfall along the front is indicated by the stippled region), they ascended several thousand meters (Fig. 9b) over a short distance. After passing through the frontal zone, the parcels turned

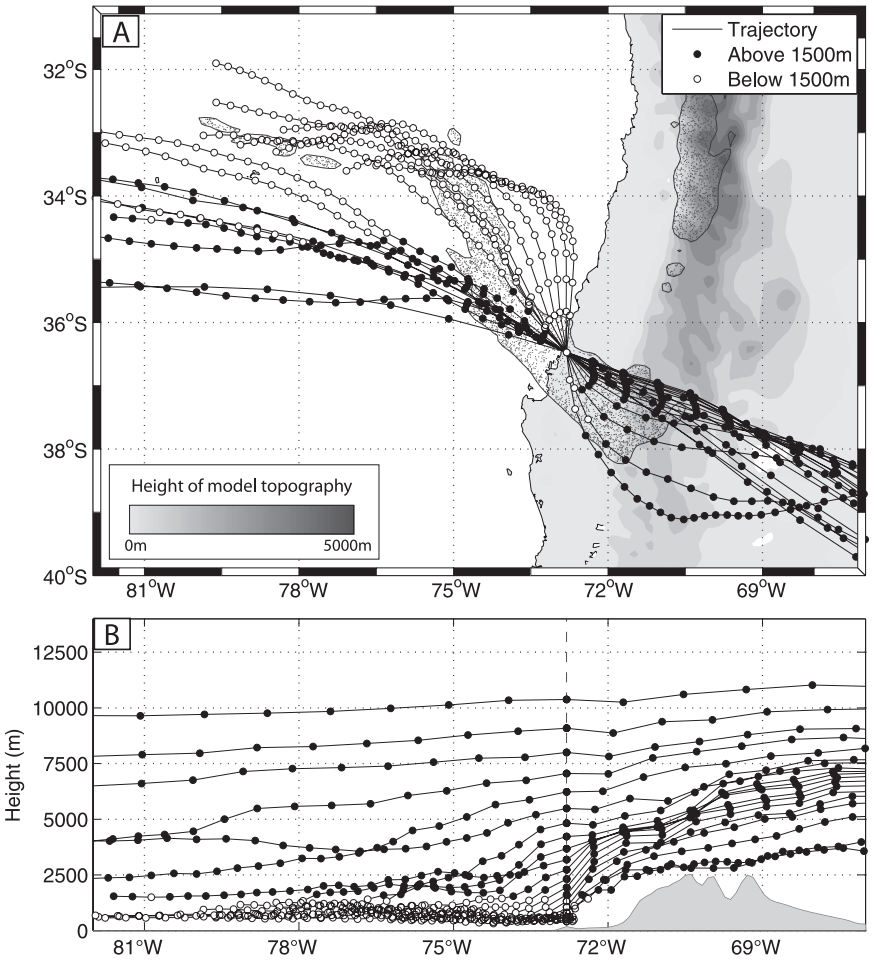

FIG. 9. Simple advective trajectory analysis showing locations of all parcels that passed through a point located just north of the synoptic cold front at 1800 UTC 26 May. Open (filled) circles represent hourly parcel locations below (above) 1500 m, and in (a), model 3-h rainfall is stippled and terrain height is shaded. The cluster of sub-1500-m parcels arriving at the cold front from the north represents the barrier jet.

eastward with the prevailing flow and continued across the southern cordillera into Argentina. The parcels located above 1500 m approached generally from the west, following the prevailing mid- and upper-level flow (Fig. 9a, closed circles), and also converged and ascended upon reaching the front. We believe the CPZ trajectories confirm the role of the barrier jet as a ''transport agent,'' moving low-level parcels from their origin in the moist southeast Pacific boundary layer to the coast. Once reaching the front, the moist parcels converged (Fig. 8b), quickly ascended, and produced heavy rainfall in the CPZ.

Farther north in the WPZ, the trajectories reveal additional information about the character and source of the region of orographic precipitation. Apart from a few parcels that appear to have been entrained in the flow from the lower troposphere, nearly all of the flow that crossed the Cordillera originated above 2500 m (Fig. 10b), including those few parcels whose trajectories brought them from the north and northwest (Fig. 10a). This result agrees with a Froude number analysis of the flow for this region, where Froude numbers greater than 1.0 (less than 1.0), which are favorable for cross-barrier (blocked) flow, were common above (below) 700 hPa. The characteristic Froude number for parcels below 700 hPa, using a scale height of 4 km and moist static stability, was 0.4, indicating the low-level flow was blocked by the topography. As the flow approached the cordillera, parcels began ascending several hundred kilometers west of the coast, and the parcels below 3500 m (open circles) that originated over the northern coast transported midlevel moisture that contributed to the orographic precipitation. In addition, it appears that the ascent of midtroposphere parcels as they approached

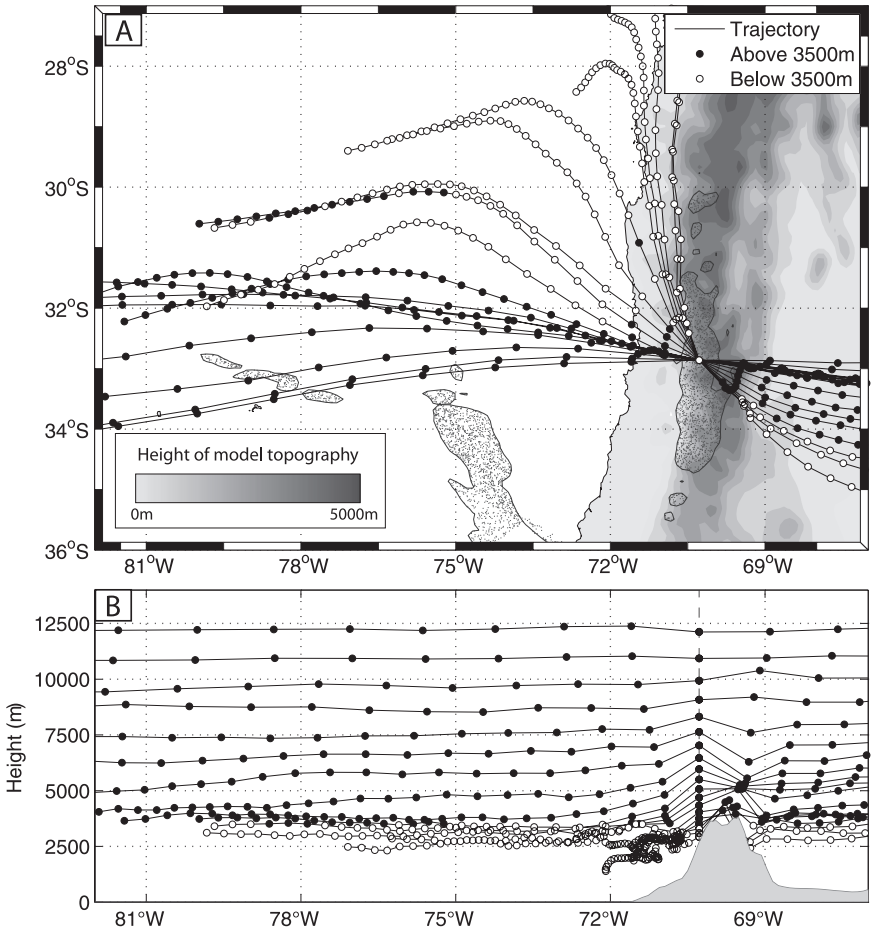

FIG. 10. As in Fig. 9, but for a point over the cordillera. Open circles represent parcels below 3500 m. Nearly all parcels that cross the barrier originate at or above 2500 m, indicating the presence of strong blocking for parcels below 700 hPa.

the cordillera from the west, including those above 3500 m (closed circles), augmented precipitation totals over the central Chilean valley, including at Santiago. These trajectory analyses are in strong agreement with the trajectory analysis of Garvert et al. (2007; their Fig. 9a), who examined a period of heavy prefrontal orographic precipitation over the Cascade Mountains of Oregon. Similar to our findings over the Andes, they documented low-level flow parallel to the topographic barrier and midlevel cross-barrier flow that originated from a different air mass region.

d. Evolution of the LOW simulation

For additional insight into the role of the Andean topography in the evolution of the frontal passage, we reran the CTL simulation with topography reduced to 20% of the original. The change in topography had little impact on the large-scale mid- and upper-level synoptic development. However, the evolution of the surface fronts and their associated precipitation was markedly different in the two simulations. There were three main differences identified in the structure and evolution of the precipitation features (Fig. 11). First, the PPZ and CPZ both advanced equatorward faster in the LOW (Figs. 11a–d) than in the CTL (Figs. 5a–d). Specifically, the PPZ reached 28°S about 12 h earlier in the LOW (Fig. 11c) than in the CTL (Fig. 5d), and the CPZ did not stall over central Chile but instead moved steadily northeastward, crossing into Argentina during the simulation. The surface front itself also advanced northeastward much more rapidly in the LOW than in the CTL, reaching the edge of the model domain about 12 h earlier than the CTL (Fig. 11). As it advanced equatorward, it maintained its shape, even across the continent (Figs. 11b,c), and did not deform as it encountered the topography. This difference is seen clearly by comparing the slopes of the CPZ in the east–west (Figs. 6a and 12a) and north–south (Figs. 6b and 12b)

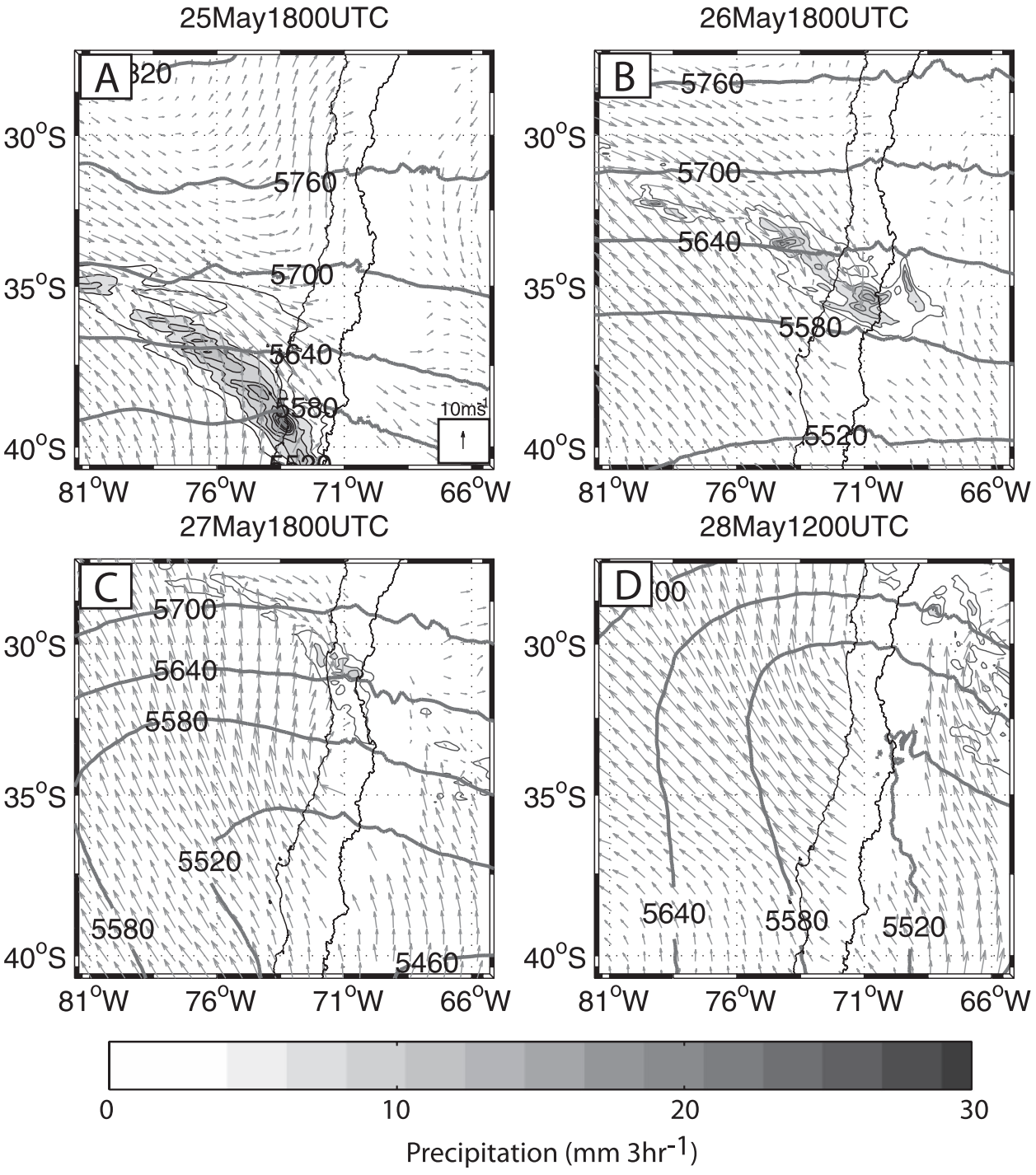

FIG. 11. As in Fig. 5, but for the LOW simulation. Note that the only precipitation feature in the LOW simulation is the PPZ, located east of the coast; the orographic WPZ does not form without high terrain.

cross sections: the isohyets have a larger slope in the CTL than in the LOW, indicating that the CPZ moved equatorward more rapidly in the LOW experiment. This deformation appears to be forced by the barrier jet. Second, precipitation intensities of the CPZ, particularly over central Chile between 33°S and 36°S, were much lower in the LOW (Fig. 12b) compared to the CTL (Fig. 6b), indicating that the total forcing for precipitation was much weaker in the LOW experiment. This difference is also reflected in storm-total precipitation (Fig. 13), where

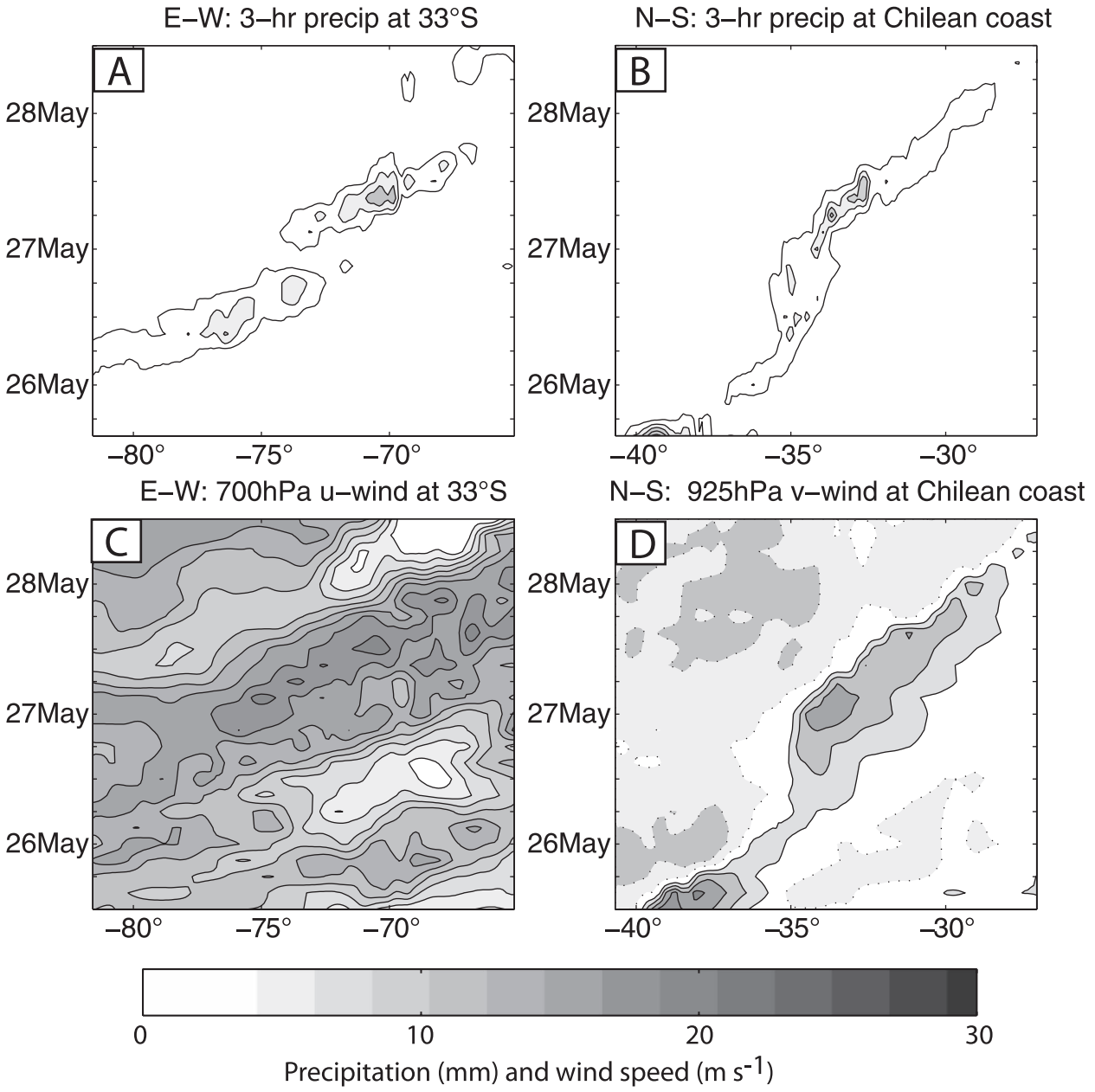

FIG. 12. LOW simulation cross sections of (a) east–west 3-h precipitation (mm) along 33°S; (b) north–south 3-h precipitation (mm) along the coast; (c) east–west 700-hPa u wind along 33°S (m s^{-1}); and (d) north–south coastal 925-hPa v wind (m s^{-1}). Wind speed in (c) and (d) is shaded every 5 m s^{-1}. In (d), stippled contours indicate southerly flow.

precipitation was much greater in the CTL than in the LOW simulation and was concentrated between 33°S and 36°S. The LOW simulation captured neither the magnitude of either the coastal and valley rainfall between 36° and 39°S nor the heavy precipitation along the cordillera. This difference in precipitation totals between the two simulations was directly related to topography: as the northerly barrier jet slows the front's equatorward progress, the jet increases convergence over the frontal slope, thus producing heavier precipitation (because of the greater convergence) that lasts longer (because of the slower frontal progression). Third, the WPZ, one of the three major precipitation features visible the CTL simulation, was completely absent from the LOW experiment (Figs. 12a and 13a), indicating that the reduced topography was not high enough to generate significant orographic precipitation. These three differences clearly demonstrate that the high Andean terrain had a significant

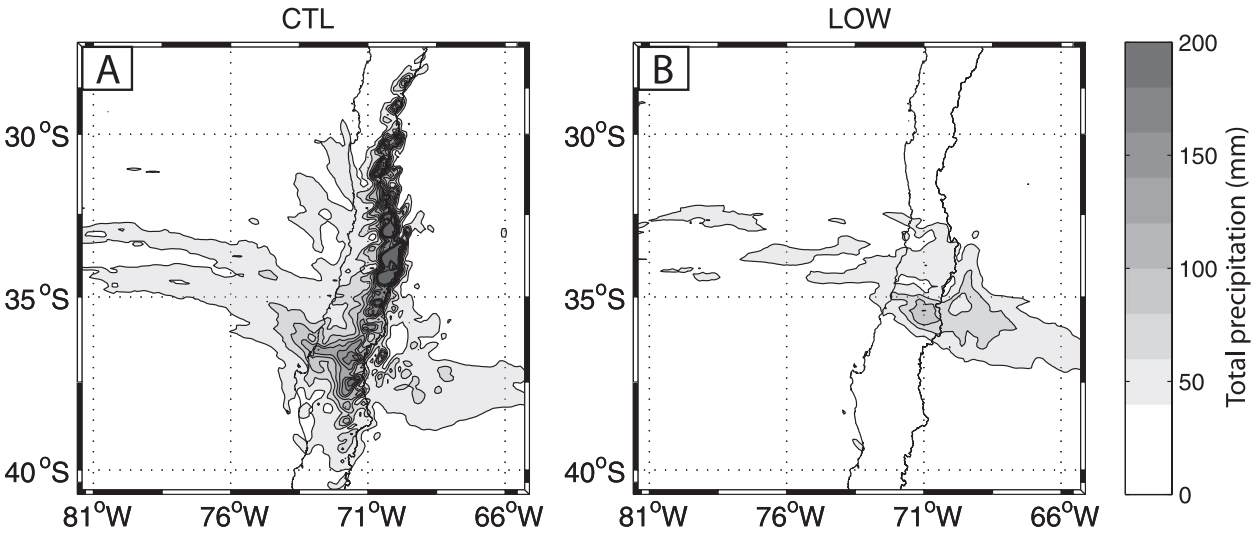

FIG. 13. Total precipitation from the (a) CTL and (b) LOW simulations.

impact on both the structure and the magnitude of frontal precipitation features in central Chile.

5. Conclusions and discussion

The goal of this study was to improve understanding of precipitation patterns in central Chile during a cold front passage and to examine the influence of the Andes on the amount and distribution of rainfall. To achieve this goal, we simulated an event from 25–28 May 2008 with both full and reduced topography. The event produced widespread precipitation over central Chile, with totals between 40 and 80 mm at coastal and valley locations increasing to over 150 mm in the precordillera. Through a combination of surface measurements, satellite observations, and numerical simulations, we identified three precipitation features and categorized them by their location (Pacific, coastal, or orographic). Trajectories over the cordillera revealed that nearly all the parcels crossing the high Andes barrier north of 35°S originated above 700 hPa, consistent with the Froude number profile of the approaching air mass. Sub-700-hPa flow was largely blocked by the topography and subsequently led to the formation of a northerly barrier jet. Farther south, trajectories calculated at points originating over the cold front indicate that the barrier jet transported moist air from the subtropical oceanic marine boundary layer southward along the Chilean coast an then up and over the frontal surface, enhancing convergence and rainfall over central and southern Chile. When topography was reduced, we found that the character of the precipitation changed dramatically. The cold front advanced more rapidly to the north and northeast, greatly reducing precipitation in the central valley between 33° and 36°S and eliminating all of the precipitation along the cordillera and most of the coastal precipitation south of 36°.

We propose the following physical mechanism to explain the precipitation pattern and role of Andean topography. As the upper-level trough approached central Chile, low-tropospheric flow was blocked by the high topography and deflected poleward in the form of a barrier jet. This northerly jet intersected the near-coast section of the cold front as it approached from the south, producing two related effects. First, the northerly flow increased convergence along the frontal surface, producing widespread rainfall totals of 40 to 80 mm over the region between 33° and 39°S. Second, the northerly flow impinged on the frontal surface and slowed its equatorward progress, causing the front to deform as its open-ocean section continued northward. The slowed progress of the coastal front increased the duration of low-level convergence of northerly flow along the frontal surface and thus increased rainfall over the CPZ. Midtropospheric flow was able to cross the topography and subsequently produced up to 300 mm of orographic precipitation along the cordillera.

Finally, precipitation totals from the LOW simulation were significantly lower than observed at nearly all of the 41 observing stations, and they were also much lower than totals from the CTL simulation. We therefore conclude that the high topography significantly augmented precipitation during this cold front passage through central Chile. The topography was directly responsible for orographic precipitation along the Cordillera, and by sustaining enhanced convergence in the meridional component of the flow at the front, it also substantially increased precipitation totals over the central coast and valley.

Acknowledgments. This project was funded by the CONICYT project ACT-19. The authors are very appreciative for the helpful comments of three anonymous reviewers and Dr. Dave Schultz, as their collective comments and suggestions have greatly improved the manuscript. We also thank Direccion de Aguas of Chile, and Mr. Dan Dawson of the University of Oklahoma, for providing access to rainfall datasets.

REFERENCES

Bell, G. D., and L. F. Bosart, 1988: Appalachian cold-air damming. *Mon. Wea. Rev.,* **116,** 137–161.

Bjerknes, J., and H. Solberg, 1921: Meteorological conditions for the formation of rain. *Geofys. Publ.,* **2,** 1–60.

Bond, N. A., B. F. Smull, M. T. Stoelinga, C. P. Woods, and A. Haase, 2005: Evolution of a cold front encountering steep quasi-2D terrain: Coordinated aircraft observations on 8–9 December 2001 during IMPROVE-2. *J. Atmos. Sci.,* **62,** 3559–3579.

Bousquet, O., and B. F. Smull, 2006: Observed mass transports accompanying upstream orographic blocking during MAP IOP8. *Quart. J. Roy. Meteor. Soc.,* **132,** 2393–2413.

Braun, S. A., R. Rotunno, and J. B. Klemp, 1999: Effects of coastal orography on landfalling cold fronts. Part I: Dry, inviscid dynamics. *J. Atmos. Sci.,* **56,** 517–533.

Buzzi, A., N. Tartaglione, and P. Malguzzi, 1998: Numerical simulations of the 1994 Piedmont flood: Role of orography and moist processes. *Mon. Wea. Rev.,* **126,** 2369–2383.

Caplan, P., and H.-L. Pan, 2000: Changes to the 1999 NCEP operational MRF/AVN analysis/forecast system. NOAA–NWS Tech. Procedures Bull. 452, 15 pp.

Chen, F., and J. Dudhia, 2001: Coupling an advanced land surface–hydrology model with the Penn State–NCAR MM5 modeling system. Part I: Model implementation and sensitivity. *Mon. Wea. Rev.,* **129,** 569–585.

Chou, M.-D., and M. J. Suarez, 1994: An efficient thermal infrared radiation parameterization for use in general circulation models. NASA Tech. Memo. 104606, Vol. 3, 85 pp.

Cox, J. A. W., W. J. Steenburgh, D. E. Kingsmill, J. C. Shafer, B. A. Colle, O. Bousquet, B. F. Smull, and H. Cai, 2005: The kinematic structure of a Wasatch Mountain winter storm during IPEX IOP3. *Mon. Wea. Rev.,* **133,** 521–542.

DiMego, G. J., L. F. Bosart, and G. W. Endersen, 1976: An examination of the frequency and mean conditions surrounding frontal incursions into the Gulf of Mexico and Caribbean Sea. *Mon. Wea. Rev.,* **104,** 709–718.

Doyle, J. D., 1997: The influence of mesoscale orography on a coastal jet and rainband. *Mon. Wea. Rev.,* **125,** 1465–1488.

——, and T. T. Warner, 1993: A three-dimensional numerical investigation of a Carolina coastal low-level jet during GALE IOP 2. *Mon. Wea. Rev.,* **121,** 1030–1047.

——, and N. A. Bond, 2001: Research aircraft observations and numerical simulations of a warm front approaching Vancouver Island. *Mon. Wea. Rev.,* **129,** 978–998.

Ebuchi, N., H. C. Graber, and M. J. Caruso, 2002: Evaluation of wind vectors observed by QuikSCAT/SeaWinds using ocean buoy data. *J. Atmos. Oceanic Technol.,* **19,** 2049–2062.

Egger, J., and K. P. Hoinka, 1992: Fronts and orography. *Meteor. Atmos. Phys.,* **48,** 3–36.

Falvey, M., and R. Garreaud, 2007: Wintertime precipitation episodes in central Chile: Associated meteorological conditions and orographic influences. *J. Hydrometeor.,* **8,** 171–193.

Farías, M., R. Charrier, S. Carretier, J. Martinod, A. Fock, D. Campbell, J. Cáceres, and D. Compte, 2008: Late Miocene high and rapid surface uplift and its erosional response in the Andes of central Chile (33°S–35°S). *Tectonics,* **27,** TC1005, doi:10.1029/2006TC002046.

Fuenzalida, H., 1982: A country of extreme climate (in Spanish). *Chile: Essence and Evolution,* H. Garcia, Ed., Instituto de Estudios Regionales, Universidad de Chile, 27–35.

Garreaud, R. D., 2000: Cold air incursions over subtropical South America: Mean structure and dynamics. *Mon. Wea. Rev.,* **128,** 2544–2559.

——, 2007: Precipitation and circulation covariability in the extratropics. *J. Climate,* **20,** 4789–4797.

——, and H. A. Fuenzalida, 2007: The influence of the Andes on cutoff lows: A modeling study. *Mon. Wea. Rev.,* **135,** 1596–1613.

——, J. Rutllant, and H. Fuenzalida, 2002: Coastal lows along the subtropical west coast of South America: Mean structure and evolution. *Mon. Wea. Rev.,* **130,** 75–88.

Garvert, M. F., B. Smull, and C. Mass, 2007: Multiscale mountain waves influencing a major orographic precipitation event. *J. Atmos. Sci.,* **64,** 711–737.

Hoskins, B. J., and K. I. Hodges, 2005: A new perspective on Southern Hemisphere storm tracks. *J. Climate,* **18,** 4108–4129.

James, C. N., and R. A. Houze, 2005: Modification of precipitation by coastal orography in storms crossing northern California. *Mon. Wea. Rev.,* **133,** 3110–3131.

Janjić, Z. I., 1996: The surface layer parameterization in the NCEP Eta model. Preprints, *11th Conf. on Numerical Weather Prediction,* Norfolk, VA, Amer. Meteor. Soc., 354–355.

——, 2001: Nonsingular implementation of the Mellor–Yamada level 2.5 scheme in the NCEP Meso model. NCEP Office Note 437, 61 pp. [Available online at http://www.emc.ncep.noaa.gov/officenotes/newernotes/on437.pdf.]

——, 2002: A nonhydrostatic model based on a new approach. Proc. EGS XVIII General Assembly, Nice, France, European Geophysical Society, Abstract 6660.

Kain, J. S., and J. M. Fritsch, 1993: Convective parameterization for mesoscale models: The Kain–Fritsch scheme. *The Representation of Cumulus Convection in Numerical Models, Meteor. Monogr.,* No. 46, Amer. Meteor. Soc., 165–170.

Kalnay, E., and Coauthors, 1996: The NCEP/NCAR 40-Year Reanalysis Project. *Bull. Amer. Meteor. Soc.,* **77,** 437–471.

Kummerow, C., W. Barnes, T. Kozu, J. Shiue, and J. Simpson, 1998: The Tropical Rainfall Measuring Mission (TRMM) sensor package. *J. Atmos. Oceanic Technol.,* **15,** 809–817.

Kurz, M., 1990: The influence of the Alps on structure and behaviour of cold fronts over southern Germany. *Meteor. Atmos. Phys.,* **43,** 61–68.

Lackmann, G. M., and J. E. Overland, 1989: Atmospheric structure and momentum balance during a gap-wind event in Shelikof Strait, Alaska. *Mon. Wea. Rev.,* **117,** 1817–1833.

Leslie, L. M., B. W. Buckley, and M. Leplastrier, 2008: The operational impact of QuikSCAT winds in Perth, Australia: Examples and limitations. *Wea. Forecasting,* **23,** 183–193.

Lin, Y.-L., R. D. Farley, and H. D. Orville, 1983: Bulk parameterization of the snow field in a cloud model. *J. Appl. Meteor.,* **22,** 1065–1092.

Lupo, A. R., J. J. Nocera, L. F. Bosart, E. G. Hoffman, and D. J. Knight, 2001: South American cold surges: Types, composites, and case studies. *Mon. Wea. Rev.,* **129,** 1021–1041.

Marwitz, J. D., 1987: Deep orographic storms over the Sierra Nevada. Part I: Thermodynamic and kinematic structure. *J. Atmos. Sci.,* **44,** 159–173.

Mass, C. F., and G. K. Ferber, 1990: Surface pressure perturbations produced by an isolated mesoscale topographic barrier. Part I: General characteristics and dynamics. *Mon. Wea. Rev.,* **118,** 2579–2596.

Medina, S., and R. A. Houze, Jr., 2003: Air motions and precipitation growth in alpine storms. *Quart. J. Roy. Meteor. Soc.,* **129,** 345–371.

Mellor, G. L., and T. Yamada, 1982: Development of a turbulence closure model for geophysical fluid problems. *Rev. Geophys.,* **20,** 851–875.

Mlawer, E. J., S. J. Taubman, P. D. Brown, M. J. Iacono, and S. A. Clough, 1997: Radiative transfer for inhomogeneous atmospheres: RRTM, a validated correlated-*k* model for the longwave. *J. Geophys. Res.,* **102,** 16 663–16 682.

Montecinos, A., and P. Aceituno, 2003: Seasonality of the ENSO-related rainfall variability in central Chile and associated circulation anomalies. *J. Climate,* **16,** 281–296.

Neiman, P. J., P. O. G. Persson, F. M. Ralph, D. P. Jorgensen, A. B. White, and D. E. Kingsmill, 2004: Modification of fronts and precipitation by coastal blocking during an intense landfalling winter storm in southern California: Observations during CALJET. *Mon. Wea. Rev.,* **132,** 242–273.

O'Handley, C., and L. F. Bosart, 1996: The impact of the Appalachian Mountains on cyclonic weather systems. Part I: A climatology. *Mon. Wea. Rev.,* **124,** 1353–1373.

Overland, J. E., 1984: Scale analysis of marine winds in straits and along mountainous coasts. *Mon. Wea. Rev.,* **112,** 2530–2534.

——, and N. A. Bond, 1993: The influence of coastal orography: The Yakutat storm. *Mon. Wea. Rev.,* **121,** 1388–1397.

——, and ——, 1995: Observations and scale analysis of coastal wind jets. *Mon. Wea. Rev.,* **123,** 2934–2941.

Parish, T. R., 1982: Barrier winds along the Sierra Nevada mountains. *J. Appl. Meteor.,* **21,** 925–930.

Pierrehumbert, R. T., and B. Wyman, 1985: Upstream effects of mesoscale mountains. *J. Atmos. Sci.,* **42,** 977–1003.

Roe, G. H., 2005: Orographic precipitation. *Annu. Rev. Earth Planet. Sci.,* **33,** 645–671.

Rotunno, R., and R. Ferretti, 2001: Mechanisms of intense Alpine rainfall. *J. Atmos. Sci.,* **58,** 1732–1749.

Seluchi, M. E., R. D. Garreaud, F. A. Norte, and A. C. Saulo, 2006: Influence of the subtropical Andes on baroclinic disturbances: A cold front case study. *Mon. Wea. Rev.,* **134,** 3317–3335.

Simpson, J., C. Kummerow, W.-K. Tao, and R. Adler, 1996: On the Tropical Rainfall Measuring Mission (TRMM). *Meteor. Atmos. Phys.,* **60,** 19–36.

Skamarock, W. C., J. B. Klemp, J. Dudhia, D. O. Gill, D. M. Barker, W. Wang, and J. G. Powers, 2005: A description of the Advanced Research WRF version 2. NCAR Tech. Note NCAR/TN-468+STR, 88 pp.

Smith, R. B., 1979a: Some aspects of the quasi-geostrophic flow over mountains. *J. Atmos. Sci.,* **36,** 2385–2393.

——, 1979b: The influence of mountains on the atmosphere. *Advances in Geophysics,* Vol. 21, Academic Press, 87–230.

——, and J. P. Evans, 2007: Orographic precipitation and water vapor fractionation over the southern Andes. *J. Hydrometeor.,* **8,** 3–19.

Trenberth, K. E., 1991: Storm tracks in the Southern Hemisphere. *J. Atmos. Sci.,* **48,** 2159–2178.

Vera, C., and Coauthors, 2006: Toward a unified view of the American monsoon systems. *J. Climate,* **19,** 4977–5000.

Winstead, N. S., and Coauthors, 2006: Using SAR remote sensing, field observations, and models to better understand coastal flows in the Gulf of Alaska. *Bull. Amer. Meteor. Soc.,* **87,** 787–800.

Yu, C.-K., and B. F. Smull, 2000: Airborne Doppler observations of a landfalling cold front upstream of steep coastal orography. *Mon. Wea. Rev.,* **128,** 1577–1603.

——, and N. A. Bond, 2002: Airborne Doppler observations of a cold front in the vicinity of Vancouver Island. *Mon. Wea. Rev.,* **130,** 2692–2708.